



UNIVERSITY OF LEEDS

This is a repository copy of *Large eddy simulation of microbubble transport in a turbulent horizontal channel flow*.

White Rose Research Online URL for this paper:
<http://eprints.whiterose.ac.uk/115728/>

Version: Accepted Version

Article:

Asiagbe, KS orcid.org/0000-0001-6957-8597, Fairweather, M, Njobuenwu, DO orcid.org/0000-0001-6606-1912 et al. (1 more author) (2017) Large eddy simulation of microbubble transport in a turbulent horizontal channel flow. *International Journal of Multiphase Flow*, 94. pp. 80-93. ISSN 0301-9322

<https://doi.org/10.1016/j.ijmultiphaseflow.2017.04.016>

© 2017 Elsevier Ltd. This manuscript version is made available under the CC-BY-NC-ND 4.0 license <http://creativecommons.org/licenses/by-nc-nd/4.0/>

Reuse

Items deposited in White Rose Research Online are protected by copyright, with all rights reserved unless indicated otherwise. They may be downloaded and/or printed for private study, or other acts as permitted by national copyright laws. The publisher or other rights holders may allow further reproduction and re-use of the full text version. This is indicated by the licence information on the White Rose Research Online record for the item.

Takedown

If you consider content in White Rose Research Online to be in breach of UK law, please notify us by emailing eprints@whiterose.ac.uk including the URL of the record and the reason for the withdrawal request.



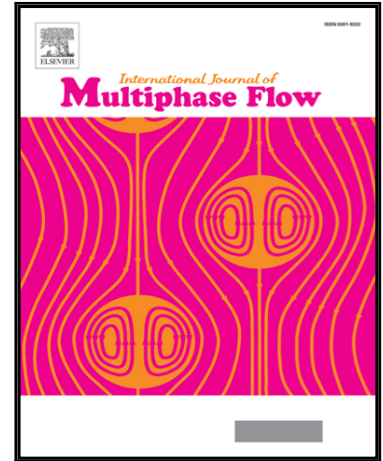
eprints@whiterose.ac.uk
<https://eprints.whiterose.ac.uk/>

Accepted Manuscript

Large eddy simulation of microbubble transport in a turbulent horizontal channel flow

Kenneth S. Asiagbe , Michael Fairweather , Derrick O. Njobuenwu , Marco Colombo

PII: S0301-9322(16)30539-0
DOI: [10.1016/j.ijmultiphaseflow.2017.04.016](https://doi.org/10.1016/j.ijmultiphaseflow.2017.04.016)
Reference: IJMF 2584



To appear in: *International Journal of Multiphase Flow*

Received date: 7 September 2016
Revised date: 24 January 2017
Accepted date: 18 April 2017

Please cite this article as: Kenneth S. Asiagbe , Michael Fairweather , Derrick O. Njobuenwu , Marco Colombo , Large eddy simulation of microbubble transport in a turbulent horizontal channel flow, *International Journal of Multiphase Flow* (2017), doi: [10.1016/j.ijmultiphaseflow.2017.04.016](https://doi.org/10.1016/j.ijmultiphaseflow.2017.04.016)

This is a PDF file of an unedited manuscript that has been accepted for publication. As a service to our customers we are providing this early version of the manuscript. The manuscript will undergo copyediting, typesetting, and review of the resulting proof before it is published in its final form. Please note that during the production process errors may be discovered which could affect the content, and all legal disclaimers that apply to the journal pertain.

Highlights

- Large eddy simulation is used to predict interacting microbubbles in a turbulent horizontal channel flow
- Two-way coupled simulations are performed based on Eulerian-Lagrangian technique
- Effects of bubble and fluid inertia on bubble migration and turbulence modulation are demonstrated
- Results are in good agreement with, and complement and extend, those obtained from direct numerical simulation

ACCEPTED MANUSCRIPT

Large eddy simulation of microbubble transport in a turbulent horizontal channel flow

Kenneth S. Asiagbe¹, Michael Fairweather, Derrick O. Njobuenwu, Marco Colombo

School of Chemical and Process Engineering, University of Leeds, Leeds LS2 9JT, UK

Abstract

Liquid-gas multiphase flows occur in many engineering and environmental applications, with the former ranging from the flow of oil and gas in pipelines, of steam and water in nuclear reactors and steam generators, and the evaporation and condensation of refrigerants in refrigeration and air conditioning equipment. In this paper, the dispersion and interaction between microbubbles and turbulence in a horizontal channel flow is investigated using a two-way coupled Eulerian-Lagrangian approach based on large eddy simulation. The microbubbles are considered to be spherical and non-deformable, and are represented by a Lagrangian bubble tracking technique, with the bubbles subject to drag, gravity, buoyancy, shear lift, added mass and pressure gradient forces. Dynamic calibration of a Smagorinsky-type sub-grid scale (SGS) closure is employed to account for the unresolved stresses, whilst a stochastic Markov method is used to describe the effect of the SGS velocity fluctuations on bubble dispersion. Channel flows of water at two shear Reynolds numbers, $Re_\tau = 150$ and 590, and three different bubble diameters, $d_b = 100, 220$ and $330 \mu m$, are simulated. The results show acceptable agreement with DNS predictions of single- and two-phase flows, with the low density microbubbles migrating towards the upper channel wall with time under the influence of buoyancy, and segregating in the upper half of the channel, with this effect increasing with bubble diameter. The accumulated bubbles near the upper wall modify the liquid velocity field, with the mean velocity profile becoming asymmetric as a consequence and with slight modification of the turbulent stresses. At higher mean velocity and turbulence levels, the buoyancy effect is reduced due to more effective turbulent dispersion of the microbubbles, leading to reduced bubble migration towards the upper channel wall.

Keywords

Large eddy simulation, Eulerian-Lagrangian, microbubbles, turbulent flow, horizontal channel

¹ Corresponding Author. E-mail: pmksa@leeds.ac.uk; Tel: +44 (0) 113 343 2351

Highlights

- Large eddy simulation is used to predict interacting microbubbles in a turbulent horizontal channel flow
- Two-way coupled simulations are performed based on Eulerian-Lagrangian technique
- Effects of bubble and fluid inertia on bubble migration and turbulence modulation are demonstrated
- Results are in good agreement with, and complement and extend, those obtained from direct numerical simulation

1. Introduction

Liquid-gas bubbly flows are frequently encountered in a wide variety of engineering, environmental and industrial applications, including boilers, distillation towers, chemical reactors, oil pipelines and nuclear reactors, amongst many others. The dynamics of bubbly flows are strongly sensitive to the flow regime, bubble size and shape, bubble velocity and void fraction, hence it is imperative to account for these parameters in order to accurately and reliably predict bubbly flow behaviour which is of importance to the operational safety, control and reliability of the type of industrial equipment noted (Hassan, 2014). Dispersed bubbly flows, where gaseous bubbles are present in a continuous liquid flow, and in general most particle-laden two-phase flows, are predicted using either Eulerian-Eulerian or Eulerian Lagrangian approaches, with attendant advantages as well as short comings (Njobuenwu et al., 2013). In this work, the Eulerian-Lagrangian approach is adopted since this method is expedient in terms of the broad motivation of our research which necessitates the accurate tracking of individual bubbles, with their subsequent coalescence due to collisions and break-up due to shear forces monitored. Hence, the subsequent discussion is limited to studies that employed this approach. In the Eulerian-Lagrangian approach, the liquid phase is treated as a continuum in the Eulerian reference frame in which the flow and turbulence are obtained by modelling or simulation, and the dispersed gas phase is treated in a Lagrangian reference frame with the individual bubbles in the system tracked by solving Newton's second law, whilst accounting for the forces acting on the bubbles.

Amongst the different types of bubbly flow, the use of microbubbles injected near a wall into a turbulent flow can generate drag reductions of up to 80%, with reductions of even small amounts being extremely beneficial to pumping and pipeline system efficiency, and skin

friction reduction on ships (Apte et al., 2003; Lu et al., 2005). Recently, a series of comprehensive reviews of drag reduction by microbubbles was published by a number of researchers (Ceccio, 2010; Murai, 2014; Paik et al., 2016; Pang et al., 2014; Watamura et al., 2013). Bubble size has been found to be a critical factor, with drag reduction only possible when the bubble diameter is less than about 1 mm, and with drag reduction rates generally higher with smaller bubble diameters.

As demonstrated by several studies of bubbly flows, the effect of bubbles and microbubbles on the liquid velocity and turbulence field is extremely complicated and depends on many factors, such as the bubble size and shape, void fraction, gas and liquid velocities, and the flow direction of the liquid (Kitagawa et al., 2005; Wang and Maxey, 1993). Bubbles experience a transverse lift force when moving in a shear or rotational flow, and this plays a decisive role in the lateral distribution of these bubbles in pipes and other industrial flows. In upflow, bubbles move faster than the liquid and, as long as their shape remains close to spherical, they are pushed towards the wall by the lift force. Here, when the bubbles are very close to the wall, the flow of liquid between the bubbles and the wall generates a wall lubrication force that tends to keep the bubbles from contacting the wall (Giusti et al., 2005; Molin et al., 2012). In downflow, the bubbles move slower than the liquid and are pushed towards the centre of the flow and away from the walls (Wang et al., 1987). In addition, when the diameter of a bubble increases beyond a certain value, deformation of the bubble by the inertia of the surrounding liquid can alter the fluid circulation around it, changing the sign of the lift force that consequently pushes the bubble, in upflow conditions, towards the centre of the flow (Ervin and Tryggvason, 1997). Several extensive studies have been carried out on the lift force (Auton, 1987; Auton et al., 1988; Lighthill, 1956) and numerous correlations for this force proposed (Hibiki and Ishii, 2007), among which is the model of Legendre and Magnaudet (1997) that is used in the present work. Nevertheless, the motion of bubbles in turbulent flows and near walls continues to be a topic of considerable interest, as shown by recent studies (de Vries et al., 2002; Jeong and Park, 2015) that considered how the trajectories of bubbles near walls change with bubble size. For relatively low Reynolds numbers, buoyant microbubbles generally rise unsteadily, with repeated interactions between the bubbles occurring (de Vries et al., 2002). This trend is, however, statistically steady and the average motion (averaged over time and space) does not change with time.

But in many practical applications (Wörner, 2012), the Reynolds number is considerably higher and bubbles at high enough Reynolds numbers rise unsteadily, either wobbling as they rise or rising along a spiral path. The direct numerical simulation (DNS) studies of Esmaeeli et al. (1994) found that two-dimensional bubbles in periodic domains start to wobble at much lower rise Reynolds numbers than their three-dimensional counterparts, and that bubbles slow down significantly once they start to wobble. Göz et al. (2002) also observed a chaotic motion for real (three-dimensional) deformable bubbles rising at high enough Reynolds numbers. However, since air bubbles are deformed to a spherical-cap shape only when their diameter is higher than a critical value, such motions might not be observed under normal conditions. From experimental work, Ellingsen and Risso (2001) suggested that the wobbling mode may be a transitional phase and that wobbly bubbles could eventually rise along spiral paths, if sufficient time were allowed.

Direct numerical simulations of such flows, with homogeneous bubble distributions in fully periodic domains, have been used to obtain results for the bubble rise velocity, velocity fluctuations, and the average relative orientation of bubble pairs (Ferrante and Elghobashi, 2004; Giusti et al., 2005; Mazzitelli et al., 2003; Molin et al., 2012; Pang et al., 2014). Xu et al. (2002) obtained results that increased understanding of turbulent boundary layers laden with microbubbles. Esmaeeli and Tryggvason (1998) used DNS to examine the motion of up to 324 two-dimensional, or 8 three-dimensional, rising bubbles at low Reynolds numbers, similar to those typical of Stokes flows. The results show that a regular bubble array is unstable and that it breaks up in two-bubble interactive systems. At low Reynolds numbers, in agreement with Stokes flow predictions, a freely evolving bubble array rose faster than a regular one, with this trend reversed at higher Reynolds numbers. Due to the rapid increase in the computational resources required to perform such simulations with Reynolds number, however, such studies are mainly limited to low Reynolds number flows. Whilst most of the research on channel flows has been focused on the use of DNS, different authors have employed large eddy simulation (LES) coupled with a Lagrangian bubble tracker to study hydrodynamics, coalescence and break-up in bubbly flows, mainly in square cross-section bubble columns (Delnoij et al., 1997; Deen et al., 2001; van den Hengel et al., 2005; Lau et al., 2014). Instead, in this work, large eddy simulation is used to study the flow of microbubbles in a horizontal channel, with specific consideration of bubble interaction with the turbulent flow, as part of an ongoing development of high accuracy computational fluid dynamic tools of value to the prediction of industrial flows. In LES, filtered forms of the

Navier-Stokes equations are solved, with only the large scales of turbulent motion resolved, whereas the sub-grid turbulent scales and their effect on the mean flow are modelled. In liquid-gas flows, the large scale turbulent structures interact with bubbles and are responsible for the macroscopic bubble motion, while small scale turbulent structures only affect small scale bubble fluctuations. Since large energy-containing motions are explicitly captured in LES, and the less energetic small scales are modelled using a sub-grid scale (SGS) model, LES can reasonably reproduce the statistics of bubble-induced velocity fluctuations in the liquid. The LES code is coupled with a Lagrangian bubble tracker and extended to study the dynamics of microbubbles in turbulent channel flows. Given the basis of the predictive methods noted, the overall approach can be expected to properly describe the scales which are responsible for the interactions between the continuous and dispersed phases and, at the same time, to permit subsequent extension to other more complex flows of engineering interest because the overall approach is less-demanding in terms of computational resources than DNS-based methods. The results described are of benefit in improving our understanding of bubbly flows, and hence are relevant to the understanding of more complex industrial flows.

The overall model is applied to the flow of air microbubbles in a horizontal water channel flow. Results are validated against the DNS results of Pang et al. (2014) at a shear Reynolds number, $Re_\tau = 150$ and a microbubble diameter, $d_b = 220 \mu\text{m}$. Additional simulations are made at the higher shear Reynolds number of $Re_\tau = 590$ to study the effect of higher turbulence levels on bubble concentration towards the upper wall promoted by buoyancy, and the modifications induced by the presence of these bubbles in the continuous phase field. Also, two additional bubble sizes ($d_b = 110$ and $330 \mu\text{m}$) are considered at both shear Reynolds numbers to investigate the complex mutual interactions between turbulence, bubble diameter and preferential bubble concentration near the upper wall. The work described forms the basis for further extensions of the overall model to handle more complex phenomena such as bubble deformation, collision, break-up and coalescence, the full implementation of which will allow the model to be deployed to study a wide range of industrially relevant flows. An illustration of how the model can be extended to address bubble coalescence is also included in this work. The paper is structured as follows. Section 2 describes the numerical model, with details of the numerical solution given in Section 3. In

Section 4, the results of the simulations are presented and discussed, with concluding remarks in the final section.

2. Mathematical Modelling

2.1 Large eddy simulation

To compute the carrier flow field, large eddy simulation was adopted. In LES, the fluid flow field is decomposed into large scale motions that are resolved by the computation, and small scale, sub-grid fluctuations by use of a filtering operation. The resolved flow field is obtained taking into account the effects of the SGS fluctuations according to the filtered continuity and momentum equations:

$$\frac{\partial \bar{u}_i}{\partial x_i} = 0, \quad (1)$$

$$\frac{\partial \bar{u}_i}{\partial t} + \bar{u}_j \frac{\partial \bar{u}_i}{\partial x_j} = -\frac{1}{\rho} \frac{\partial \bar{p}}{\partial x_i} - \frac{\partial}{\partial x_j} (\bar{\sigma}_{ij} + \tau_{ij}) + \frac{\bar{\Delta p}}{\rho L_z} \delta_{i3} + \frac{f_{2w,i}}{\rho}, \quad (2)$$

where the overbar identifies filtered quantities, ρ is the fluid density, u the Eulerian fluid velocity, p the pressure, μ the dynamic viscosity, and σ_{ij} is the viscous stress given by:

$$\bar{\sigma}_{ij} = -2\mu \bar{S}_{ij} = -\mu \left(\frac{\partial \bar{u}_i}{\partial x_j} + \frac{\partial \bar{u}_j}{\partial x_i} \right). \quad (3)$$

Here, S_{ij} is the strain-rate tensor, and τ_{ij} in Eq. (2) is the sub-grid scale stress tensor, arising from the top-hat filtering operation, which is required to close the system of equations. The SGS stress is modelled using the dynamic model of Germano et al. (1991), implemented using the approximate localisation procedure of Piomelli and Liu (1995) together with the modification proposed by di Mare and Jones (2003), according to:

$$\tau_{ij} = \bar{u}_i \bar{u}_j - \bar{u}_i \bar{u}_j. \quad (4)$$

The dynamic SGS model is adopted here as it is a function of both space and time, and hence is more accurate than the standard Smagorinsky model which depends on choosing an optimal model constant. The SGS stresses are obtained from the product of a SGS turbulent kinematic viscosity, ν_{SGS} , and the resolved part of the strain-rate tensor. The SGS kinematic viscosity is evaluated as the product of the filter width Δ and an appropriate velocity scale:

$$\nu_{SGS} = (C\Delta)^2 \|\bar{S}\|. \quad (5)$$

with

$$\|\bar{S}\| = \sqrt{2\bar{S}_{ij}\bar{S}_{ij}}. \quad (6)$$

Therefore, the anisotropic part of the SGS stress tensor is given by:

$$\tau_{ij}^a = -2(C\Delta)^2 \|\bar{S}\| \bar{S}_{ij}. \quad (7)$$

The model coefficient C is estimated by applying a second filter, known as the test filter, denoted by \sim in the equations. In the test filtered equation the SGS stresses are:

$$T_{ij} = \overline{u_i u_j} - \tilde{u}_i \tilde{u}_j. \quad (8)$$

The parameters T_{ij} and \tilde{T}_{ij} are unknown but are related by Germano's identity (Germano et al., 1991) through the resolved stress tensor:

$$L_{ij} = T_{ij} - \tilde{T}_{ij} = \overline{u_i u_j} - \tilde{u}_i \tilde{u}_j \quad (9)$$

which can be calculated from the resolved quantities. To give the required expression for C , some form of relationship between the model constant values C and $C^2(\tilde{\bullet})$ at the grid- and test-filter levels must be specified and, based on the hypothesis that the cut-off length falls inside the inertial sub-range, $C^2 = C^2(\tilde{\bullet})$. However, such a sub-range is not guaranteed to occur in wall bounded or low Reynolds number flows, with the largest deviation from universality of the SGS motions expected to occur in the regions of weakest resolved strain. Based on this, the two values of the model parameter at two different filter levels are liable to differ. To account for this, di Mare and Jones (2003) proposed the following:

$$C^2(\tilde{\bullet}) = C^2 \left(1 + \frac{\varepsilon}{2\sqrt{2}\tilde{\Delta}^2 \|\tilde{\bar{S}}\| \|\tilde{\bar{S}}^a\|^2} \right), \quad (10)$$

where ε represents the assumed turbulence energy dissipation rate, such that $\varepsilon \approx v^3/l$, v and l are the velocity and length scales, respectively, such that $v = u_b$ and $l = h$, where u_b and h are the bulk velocity and channel half-height for the flows considered herein.

Equation (10) is based on the assumption that the scale invariance of C can only be invoked if the cut-off falls inside an inertial sub-range, and when this occurs, the modelled dissipation should represent the entire dissipation in the flow. Conversely, in the high Reynolds number limit, the dissipation is only determined by v and l so that the ratio of ε to $\tilde{\Delta}^2 \|\tilde{\bar{S}}\|^3$ is a measure of how far the flow is from scale preserving conditions. This equation represents a first-order expansion of other scale dependent expressions for C , e.g. that of Porte-Agel et al. (2000) which also use a single length and velocity scale. Equations (9) and (10) with contraction of both sides with the tensor $\tilde{\bar{S}}$, then give:

$$C^2 = \frac{\left[2\sqrt{2}(C_*^2 \Delta)^2 \|\bar{s}\| \|\bar{s}_{ij}^a\| \|\tilde{s}_{ij}^a - L_{ij}^a \tilde{s}_{ij}^a\| \right]}{\varepsilon + 2\sqrt{2}\Delta^2 \|\tilde{s}\| \|\tilde{s}^a\|^2}, \quad (7)$$

where C_*^2 is a provisional value for the field C^2 , for example, its value at the previous time step (Piomelli and Liu, 1995). The dependence embodied in Eq. (7) gives a simple correlation for C^2 . The main advantage of this method is that it is well conditioned and avoids the spiky and irregular behaviour exhibited by some implementations of the dynamic model and, as the resolved strain tends to zero, C^2 also tends to zero, while $C^2(\tilde{\bullet})$ remains bounded. The dissipation term also yields smooth C^2 fields without a need for averaging, and the maxima of C^2 are of the same order of magnitude as Lilly's (1967) estimate for the Smagorinsky model constant. Negative values of the model parameters are not prevented, with such values set to zero to prevent instability. Negative values of the SGS viscosity are similarly set to zero. In the present work, test filtering was performed in all space directions, with no averaging of the calculated model parameter field. The ratio $\tilde{\Delta}/\Delta$ was set to 2 and the filter width determined from $\Delta = (\Delta_x \Delta_y \Delta_z)^{1/3}$, where Δ_x , Δ_y , and Δ_z denotes the physical grid spacing in the three coordinate directions.

The last two terms on the right hand side of Eq. (2) represent the mean pressure gradient, $\overline{\Delta p}/L_z$, required to drive the flow and the action on the fluid of the bubbles, $f_{2w,i}$, given by the summation of all the hydrodynamic forces acting on the bubbles except gravity and buoyancy. The mean pressure gradient, taken into account gravity and buoyancy forces, is given by (Molin et al., 2012; Yamamoto et al., 2001):

$$\frac{\overline{\Delta p}}{L_z} = -\frac{\rho u_\tau^2}{h} + \alpha_b (\rho - \rho_b) g \quad (8)$$

where u_τ is the fluid shear velocity, α_b the bubble volume fraction, ρ_b the bubble density and g the acceleration due to gravity. The term $f_{2w,i}$ is considered further below.

2.2 Lagrangian tracking of bubble motion

The motion of a small rigid spherical bubble in a turbulent flow field is described by Newton's second law of motion (Maxey and Riley, 1983). With the bubble-fluid density ratio $\rho_b/\rho \ll 1$, the microbubbles are subjected to drag, lift, gravity, buoyancy, pressure gradient and added mass forces, and a stochastic contribution arising from the SGS velocity fluctuations (Elghobashi and Truesdell, 1992). The Basset history force is neglected in this

work following the observation of Rivero et al. (1991) and Sridhar and Katz (1999) that, in the case of bubbles, this force is always negligible in comparison with the other forces noted. Therefore, the motion of microbubbles obeys the following Lagrangian equation written per unit mass:

$$\frac{d\mathbf{v}}{dt} = \left(1 - \frac{\rho_l}{\rho_b}\right) \mathbf{g} + \frac{\mathbf{u} - \mathbf{v}}{\tau_b} C_{SN} + C_L \frac{\rho_l}{\rho_b} [(\mathbf{u} - \mathbf{v}) \times \boldsymbol{\omega}] + \frac{\rho_l}{\rho_b} \frac{d\mathbf{u}}{dt} + \frac{\rho_l}{2\rho_b} \left(\frac{d\mathbf{u}}{dt} - \frac{d\mathbf{v}}{dt}\right) + \chi_{sgs}, \quad (9)$$

where the terms on the right hand side of Eq. (9) represent the gravity-buoyancy, drag, shear-lift, pressure gradient and added mass forces per unit mass, respectively, while the last term, χ_{sgs} , represents the effect of the SGS velocity fluctuations on the bubble motion. Subscripts l and b represent liquid and bubble, respectively, $\boldsymbol{\omega} = 0.5 \times \nabla \mathbf{u}$ is the fluid vorticity, and τ_b is the bubble relaxation time which can be corrected to account for added mass effects to give $\check{\tau}_b = \tau_b(1 + \rho_l/2\rho_b)$. The bubble position vector x_b is obtained by further differentiation of Eq. (9).

The coefficient C_{SN} represents the non-linear Schiller and Naumann (1935) drag coefficient written, with respect to the bubble Reynolds number $Re_b = |\mathbf{u} - \mathbf{v}|d_b/\nu$, as:

$$C_{SN} = (1 + 0.15Re_b^{0.687}) \quad (10)$$

The lift coefficient C_L is also a function of Re_b and the dimensionless shear rate Sr_b , and is computed from the correlation of Legendre and Magnaudet (1997):

$$C_L = \sqrt{(C_L^{lowRe})^2 + (C_L^{highRe})^2}, \quad (11)$$

where

$$C_L^{lowRe} = \frac{6}{\pi^2} (Re_b Sr_b)^{-0.5} \left[\frac{2.255}{(1 + 0.2\xi^{-2})^{1.5}} \right] \quad (12)$$

and

$$C_L^{highRe} = \frac{1}{2} \left(\frac{1 + 16/Re_b}{1 + 29/Re_b} \right) \quad (13)$$

with $Sr_b = |\boldsymbol{\omega}|d_b/(2|\mathbf{u} - \mathbf{v}|)$ and $\xi = \sqrt{Sr_b/Re_b}$.

The last term in Eq. (9), representing the effect of the SGS velocity fluctuations on bubble motion, is determined using a stochastic Markov model (Bini and Jones, 2008) which represents the influence of the unresolved fluctuations on bubble acceleration using:

$$\chi_{sgs} = C_0 \left(\frac{k_{sgs}}{\tau_t} \right) dW_t/dt, \quad (14)$$

where k_{sgs} is the unresolved kinetic energy of the liquid phase, C_0 is a model constant taken as unity, and dW_t represents the increment of the Wiener process. During the simulation, dW_t is represented by $\xi_i \times \sqrt{\Delta t}$, where ξ_i is a random variable sampled from a normal distribution with zero mean and a variance of unity, and which is independent for each time step and for each velocity component. τ_t is a sub-grid time scale which affects the rate of interaction between the bubble and the turbulence dynamics, defined as:

$$\tau_t = \frac{\tau_b^{1.6}}{(\Delta/k_{sgs}^{0.5})^{0.6}}. \quad (15)$$

The SGS kinetic energy is obtained from $k_{sgs} = (2\Delta v_{sgs} \bar{S}_{ij} \bar{S}_{ij})^{2/3}$, an expression derived using equilibrium arguments (Bini and Jones, 2008). Interaction and collision of the bubbles with a wall are handled using the hard sphere collision model (Njobuenwu and Fairweather, 2017).

2.3 Two-way coupling

In situations where the bubble volume fraction is greater than 10^{-6} , the momentum transfer from the bubble suspension is large enough to modify the structure of the turbulence of the carrier fluid and the flow is referred to as two-way coupled. This coupling effect is enforced by the addition of the source term $f_{2w,i}$ which represents the force per unit volume exerted by the bubbles on the fluid in the fluid momentum balance equation, Eq. (2), and is given by:

$$f_{2w,i} = \frac{1}{\Delta^3} \sum_{j=1}^{n_b} f_{H,i}^j, \quad (20)$$

where the summation is defined over the number of bubbles n_b present in the computational cell volume under consideration, $f_{H,i}^j$ is the source term arising from the j^{th} bubble in the i^{th} direction, and the subscript H represents the hydrodynamic force terms. In the present case, the relevant source term for the LES momentum equation is the summation of all the hydrodynamic force terms (drag, shear-lift, pressure gradient and added mass), excepting the body force (gravity and buoyancy) terms which occur on the right hand side of Eq. (9) since these have already been included in the pressure gradient term:

$$f_{H,i}^j = -m_b \left[\frac{dv_i}{dt} - \left(1 - \frac{\rho_l}{\rho_b}\right) g_i \right], \quad (21)$$

where m_b is the mass of a bubble and $g = 9.81, 0$ and 0 ms^{-2} in the $i = x, y$ and z directions, respectively.

2.4 Four-way coupling

In the final part of the results and discussion section below, an extended version of the model is used, including a four-way coupled mechanistic approach that accounts for bubble-bubble collision and coalescence. Bubble-bubble collisions are individually tracked and, after collision, bubbles may bounce off one another or coalesce, depending on their relative velocity and radii. Collision is modelled using the deterministic, hard sphere, frictionless inter-bubble collision model, therefore collisions are binary and perfectly elastic, and deformation after collision is neglected (Breuer and Alletto, 2012; Njobuenwu and Fairweather, 2015).

After collision, the probability of coalescence is evaluated using the Prince and Blanch (1990) model, based on the film drainage approach. In this model, two bubbles that collide trap a small amount of liquid between them. For coalescence to take place, the liquid film has to drain out down to a critical thickness where rupture occurs. Therefore, coalescence occurs only when the bubble contact time τ_{ij} exceeds the film drainage time t_{ij} . Otherwise, the colliding bubbles bounce off one another without coalescence. The contact time is assumed to be given as:

$$\tau_{ij} = \frac{C_c R_{ij}}{u_n} \quad (22)$$

where R_{ij} is the equivalent bubble radius which is given as:

$$R_{ij} = 2.0 \left(\frac{2}{d_{b1}} + \frac{2}{d_{b2}} \right)^{-1} \quad (23)$$

Here, u_n is the relative approach velocity of the bubbles in the normal direction, and C_c is the deformation distance. The latter's value was taken as 0.25 as this has been found to give optimal agreement with experimental data (Sommerfeld et al., 2003). The film drainage time is expressed as (Prince and Blanch, 1990):

$$t_{ij} = \sqrt{\frac{R_{ij}^3 \rho_l}{16\sigma}} \ln \left(\frac{h_0}{h_f} \right) \quad (24)$$

with the initial film thickness h_0 for water-air set to 1.0×10^{-4} m, the final film thickness before rupture h_f set to 1.0×10^{-8} m (Prince and Blanch, 1990), the bubble surface tension σ given as $7.2 \times 10^{-2} \text{ Nm}^{-1}$, and where d_{b1} and d_{b2} are the two colliding bubble diameters. The properties of the new bubble after coalescence are calculated from a mass and momentum balance. The new bubble diameter after coalescence is calculated as:

$$d_{b,new} = (d_{b1}^3 + d_{b2}^3)^{1/3} \quad (25)$$

In further work, not reported below, it was found that at the Reynolds numbers investigated, bubble break-up was negligible.

3. Numerical Solution

Before introducing bubbles, a fully developed single-phase turbulent channel flow was obtained at shear Reynolds numbers $Re_\tau = u_\tau h / \nu$ of 150 and 590, with water as the carrier phase fluid with kinematic viscosity $\nu = 10^{-6} \text{ m}^2 \text{ s}^{-1}$ and density $\rho = 1000 \text{ kg m}^{-3}$. The computational domain is a channel bounded by two infinite flat parallel walls, as illustrated in Fig. 1, with the x , y and z axes pointing in the wall normal, spanwise and streamwise directions, respectively. A channel flow was adopted to benefit from its advantages in terms of the simplified implementation of boundary and initial conditions, as well as the reduced computation times compared to other geometries. The dimensions of the computational domain were set to $L_x \times L_y \times L_z = 2h \times 2\pi h \times 4\pi h$, and these were discretised using $N_x \times N_y \times N_z = 129 \times 128 \times 128$ grid points in the x , y and z directions, respectively. The grid nodes were distributed uniformly along the y – and z – axes, and non-uniformly using a hyperbolic function (Gamet et al., 1999) in the wall normal direction. A no-slip boundary condition is imposed at the channel walls, while periodic boundary conditions are imposed in the streamwise and spanwise directions, with the flow being driven using an imposed streamwise fixed pressure gradient. The BOFFIN (boundary fitted flow integrator) code was used to solve the governing equations. This code has been applied extensively in the LES of reacting, e.g. di Mare et al. (2004) and Jones et al. (2014), and non-reacting, e.g. Bini and Jones (2008) and Njobuenwu and Fairweather (2015) turbulent flows. For further details of the numerical methods used in BOFFIN, readers are referred to these publications and references therein.

Air bubbles with a density $\rho_b = 1.3 \text{ kg m}^{-3}$ were introduced uniformly into fully-converged single-phase flow solutions, with the initial velocity of a bubble equal to the fluid velocity at the bubble location, obtained by interpolation. Three bubble sizes, $d_b = 110, 220$ and $330 \text{ }\mu\text{m}$, were considered, and the bubble volume fraction was chosen as $\alpha_b = 1.12 \times 10^{-4}$, which is high enough to allow analysis of the effect of microbubbles on the continuous flow field but, at the same time, low enough to ensure negligible bubble – bubble interaction. This

corresponds to a total number of 181,272 microbubbles for $d_b = 110 \mu\text{m}$, 25,400 for $d_b = 220 \mu\text{m}$ and 6,714 for $d_b = 330 \mu\text{m}$.

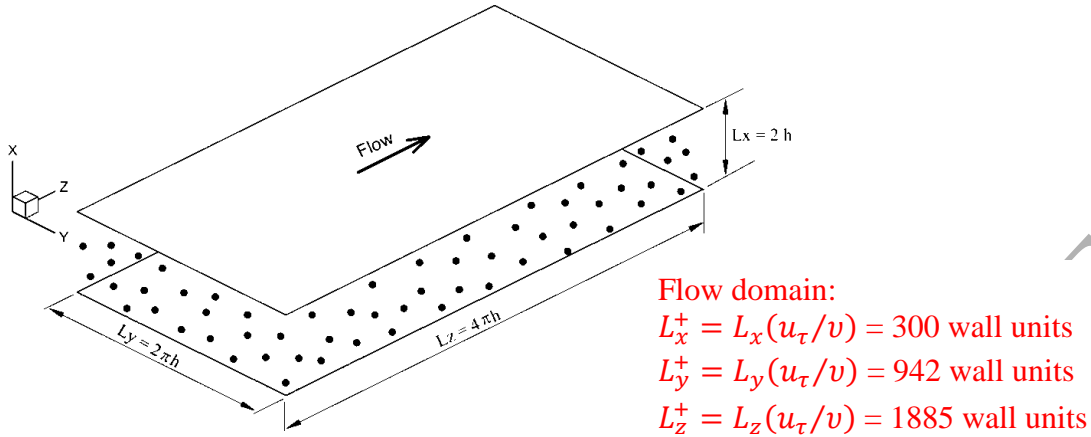


Figure 1. Coordinate system and channel geometry details.

Table 1. Computational parameters of liquid and bubbles relevant to the simulation of bubble dispersion for the two flow Reynolds numbers. Superscript + signifies dimensionless variables. $N_b = \alpha_b C_D / \text{volume of sphere}$ is the number of tracked bubbles, where C_D is volume of the flow domain.

$Re_\tau = 150$		$Re_b = 2272$		$u_\tau = 7.5 \times 10^{-3} \text{ ms}^{-1}$	$u_{bulk} = 0.114 \text{ ms}^{-1}$	
$d_b / \mu\text{m}$	d_b^+	$\tau_b / \mu\text{s}$	τ_b^+	$\tilde{\tau}_b / \text{s}$	$\tilde{\tau}_b^+$	N_b
110	0.825	0.874	4.894×10^{-5}	3.370×10^{-4}	1.895×10^{-2}	181,272
220	1.650	3.495	1.966×10^{-4}	1.349×10^{-3}	7.582×10^{-2}	25,400
330	2.475	7.865	4.424×10^{-4}	3.033×10^{-3}	1.706×10^{-1}	6,714
$Re_\tau = 590$		$Re_b = 11033$		$u_\tau = 2.9 \times 10^{-2} \text{ ms}^{-1}$	$u_{bulk} = 0.552 \text{ ms}^{-1}$	
$d_b / \mu\text{m}$	d_b^+	$\tau_b / \mu\text{s}$	τ_b^+	$\tilde{\tau}_b / \text{s}$	$\tilde{\tau}_b^+$	N_b
110	3.245	0.874	7.605×10^{-4}	3.370×10^{-4}	0.293	181,272
220	6.490	3.495	3.042×10^{-3}	1.349×10^{-3}	1.173	25,400
330	9.735	7.865	6.845×10^{-3}	3.033×10^{-3}	2.639	6,714

The trajectory of individual microbubbles was obtained from integration of the Lagrangian tracking equation, Eq. (9), which was solved using a fourth-order Runge–Kutta scheme. Perfectly elastic collisions were assumed at the walls when the microbubble centre was at a distance from the wall lower than the bubble radius. The time-step for the bubble tracker was chosen equal to that of the fluid solver time-step, and corresponding to roughly one fifth of the bubble relaxation time ($\tau_b = \rho_b d_b^2 / 18\mu$) for both Reynolds' numbers (Molin et al., 2012). τ_b can be corrected to account for added mass effects, resulting in $\tilde{\tau}_b = \tau_b(1 +$

$\rho/(2\rho_b)) \approx 358.6\tau_b$ (Molin et al., 2012). Simulation parameters are defined in Table 1. The total simulation time, which is a dimensionless time in wall units, was obtained using the expression $t^+ = t u_\tau^2 / \nu$, where t is the computational time in seconds, ν represents the fluid kinematic viscosity and u_τ^2 is the square of the shear velocity. t^+ was 200 for $Re_\tau = 150$, and 2000 for $Re_\tau = 590$, with averaging carried out after 100 and 1000 t^+ , respectively. These were found to be sufficient to ensure convergence of averaged quantities, and constant values of bubble concentration profiles. Here, and below, the superscript ($^+$) refers to a non-dimensional quantity scaled by the wall (viscous) variables, where u_τ/ν , u_τ and ν/u_τ^2 are the characteristic length, velocity and time scales. Also, t^+ values quoted relate to times after the bubbles were first introduced to the fully developed single-phase solutions.

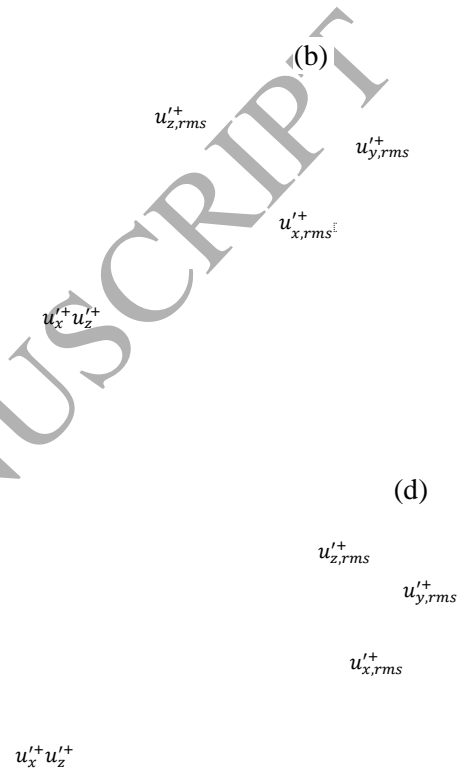
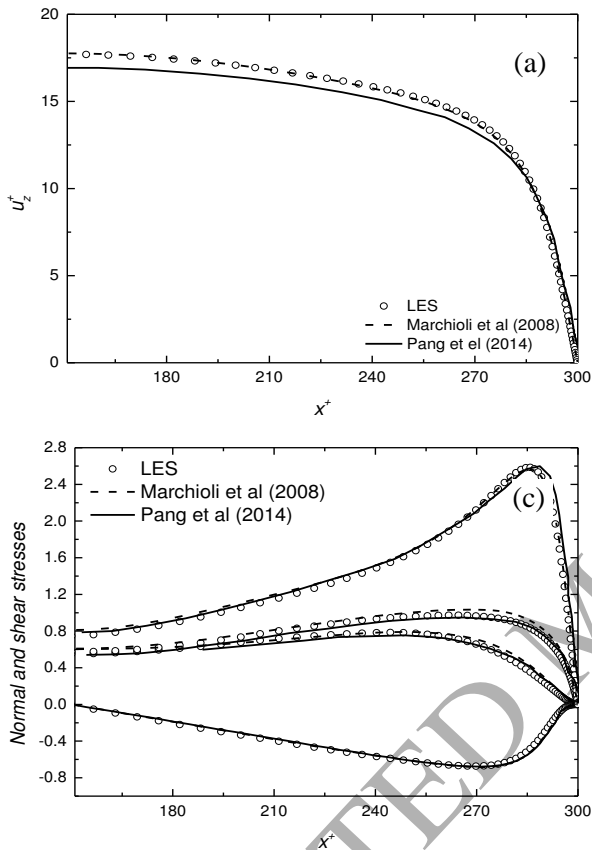
4. Results and Discussion

In this section, simulation results are discussed, and in particular the velocity fields for both the fluid and the microbubbles, as well as microbubble concentration profiles. First of all, single-phase LES results are validated against DNS predictions. The DNS results of Pang et al. (2014) are also used to validate LES simulations of the multiphase flow at $Re_\tau = 150$ and $d_b = 220 \mu\text{m}$. LES is then used to extend the simulations to $Re_\tau = 590$ and bubble diameters $d_b = 110$ and $330 \mu\text{m}$. An examination of the forces acting on the bubbles is then performed, followed by an assessment of the importance of bubble coalescence in the flows considered. Note that the fluid and bubble velocities are expressed in wall units, obtained from $u^+ = u/u_\tau$, where u is the actual velocity in ms^{-1} .

4.1 Single-phase flow

Figure 2 shows the steady profiles of the mean streamwise velocity, the root mean square (rms) of the velocity fluctuations and the $u_x'^+ u_z'^+$ shear stress at shear Reynolds numbers of 150 and 590. Here, and in the following, these profiles have been obtained after averaging over time and space. For $Re_\tau = 150$, the LES results are compared against the DNS predictions of Pang et al. (2014) that, for a $10h \times 5h \times 2h$ domain, applied a mesh resolution of $64 \times 64 \times 64$ which is less refined than the present LES. While the turbulent stresses (Fig. 2(b)) are in good agreement, the streamwise velocity is over-predicted with respect to the Pang et al. (2014) results. Therefore, to further extend the validation of the LES, the single-phase DNS results of Marchioli et al. (2008), made using the same computational domain as in the present work, are also included in the comparison. From Fig. 2(a), the LES streamwise mean velocity

profile is in rather good agreement with the Marchioli et al. (2008) DNS which also adopted the same resolution as the present LES. Therefore, the under-prediction of the mean velocity profile obtained using the LES by Pang et al. (2014) can be attributed to the grid resolution used by the latter authors. Turbulent stresses predicted by the LES remain in good agreement with those obtained by Marchioli et al. (2008).



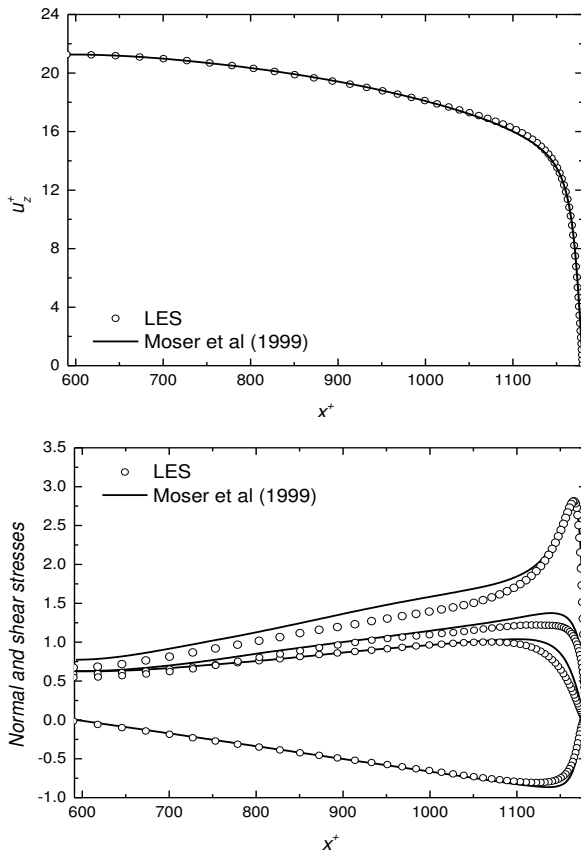


Figure 2. Single-phase velocity statistics: mean streamwise velocity (a, c) and turbulent normal and shear stresses (b, d) for $Re_\tau = 150$ (a, b) and $Re_\tau = 590$ (c, d).

In Fig. 2(c, d), the LES results at $Re_\tau = 590$ are compared against the predictions of Moser et al. (1999) who carried out DNS of channel flow at shear Reynolds numbers $Re_\tau = 180, 395$ and 590 using a spectral element numerical solution method. The LES results are in good agreement with those of Moser et al. (1999) for both the mean velocity and the turbulent stresses, although the normal stresses are slightly under-predicted near the wall in the spanwise and wall normal directions, and near the centre of the channel in the streamwise direction. Moser et al. (1999) used a grid resolution of $384 \times 257 \times 384$ in contrast to the resolution of $129 \times 128 \times 128$ used in this work. Despite the differences noted above, however, the large eddy simulations at both Reynolds numbers are in acceptable agreement with the DNS results considered for comparison purposes, with the ability of the LES to resolve the main characteristics of the turbulent flows evident. This, in the context of multiphase flows, translates into the ability of the LES to resolve the scales that are mainly responsible for fluid-bubble interactions.

4.2 Two-phase flow

In this section, a two-way coupled LES is compared with the DNS of Pang et al. (2014) at $Re_\tau = 150$ and for $d_b = 220 \mu\text{m}$. Fig. 3 shows the fluid velocity statistics, the bubble velocity statistics and bubble concentration profiles with time. Fig. 3(a, b) gives the fluid mean streamwise velocity, and turbulent normal and shear stresses. The mean streamwise velocity of Pang et al. (2014) is slightly over-predicted, probably as a consequence of the lower grid resolution used by the latter authors as noted above, although the normal and shear stress results of both approaches are in good agreement. These results are in line with those obtained for the $Re_\tau = 150$ single phase flow considered in the previous section.

Figure 3 (c, d) gives the microbubble mean velocity and turbulent stress profiles, again compared with the DNS predictions of Pang et al. (2014), where available. For the mean bubble velocity, the DNS is found to be lower than the LES results as a consequence of the under-predicted continuous phase mean velocity. Unfortunately, no DNS results for the turbulent stresses were provided by Pang et al. (2014), although the LES results are given in Fig. 3. For both the LES and the DNS, the velocity profiles of the gas and liquid phases are very similar, with the microbubble mean velocity being slightly higher than that of the fluid phase. An explanation to this is provided by Pang et al. (2014). The interphase forces acting on the microbubbles are the drag, lift, added mass, gravity-buoyancy and the pressure gradient forces. In the streamwise direction, the added mass, pressure gradient and gravity-buoyancy forces are negligible, and the drag force is expected to be weak due to the low mean slip velocity between the gas and liquid phases. The velocity difference is therefore mostly generated by the component of the lift force in the streamwise direction induced by the spanwise vorticity (Pang et al., 2014), and this effect is reproduced by the LES.

In the wall-normal direction, gravity-buoyancy is the dominant force, even if the lift force is expected to contribute towards moving the bubbles towards the channel walls. The gravity-buoyancy force itself forces the lower density bubbles towards the upper wall of the channel, and Fig. 3 (e, f) illustrates the evolution of the microbubble concentration with time. Starting from an initially uniform bubble concentration, the bubbles gradually migrate from the lower channel wall to the upper wall and, by $t^+ = 102$, the majority of the bubbles have moved close to the latter wall.

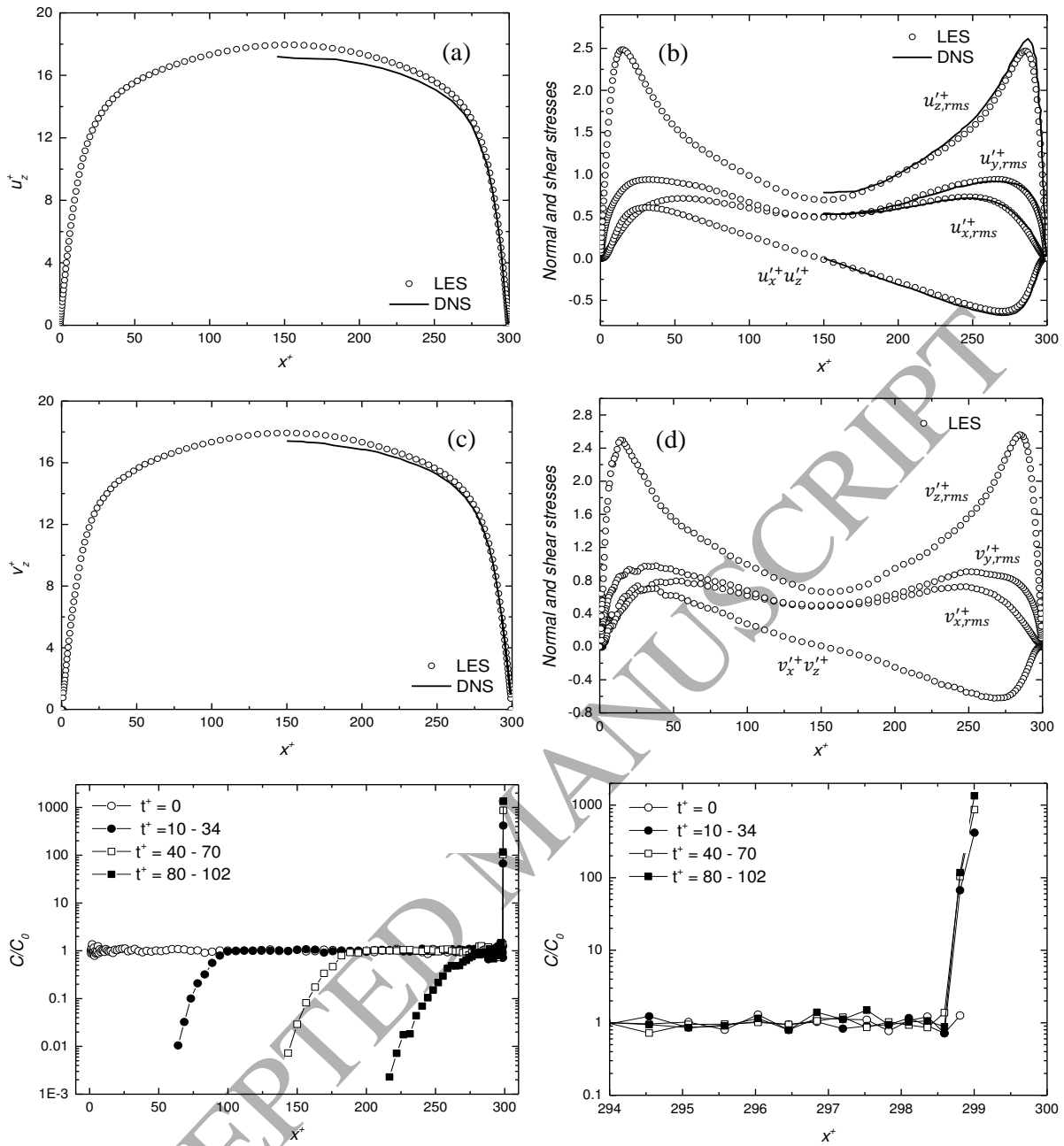


Figure 3. Fluid and bubble velocity statistics at $t^+=102$, and time evolution of bubble concentration profiles, in two-way coupled simulations compared with Pang et al. (2014) DNS at $Re_\tau = 150$: (a) fluid mean streamwise velocity, (b) fluid turbulent normal and shear stresses, (c) bubble mean streamwise velocity, (d) bubble turbulent normal and shear stresses, (e) bubble concentration profiles across the horizontal channel, and (f) bubble concentration profiles close to the upper channel wall.

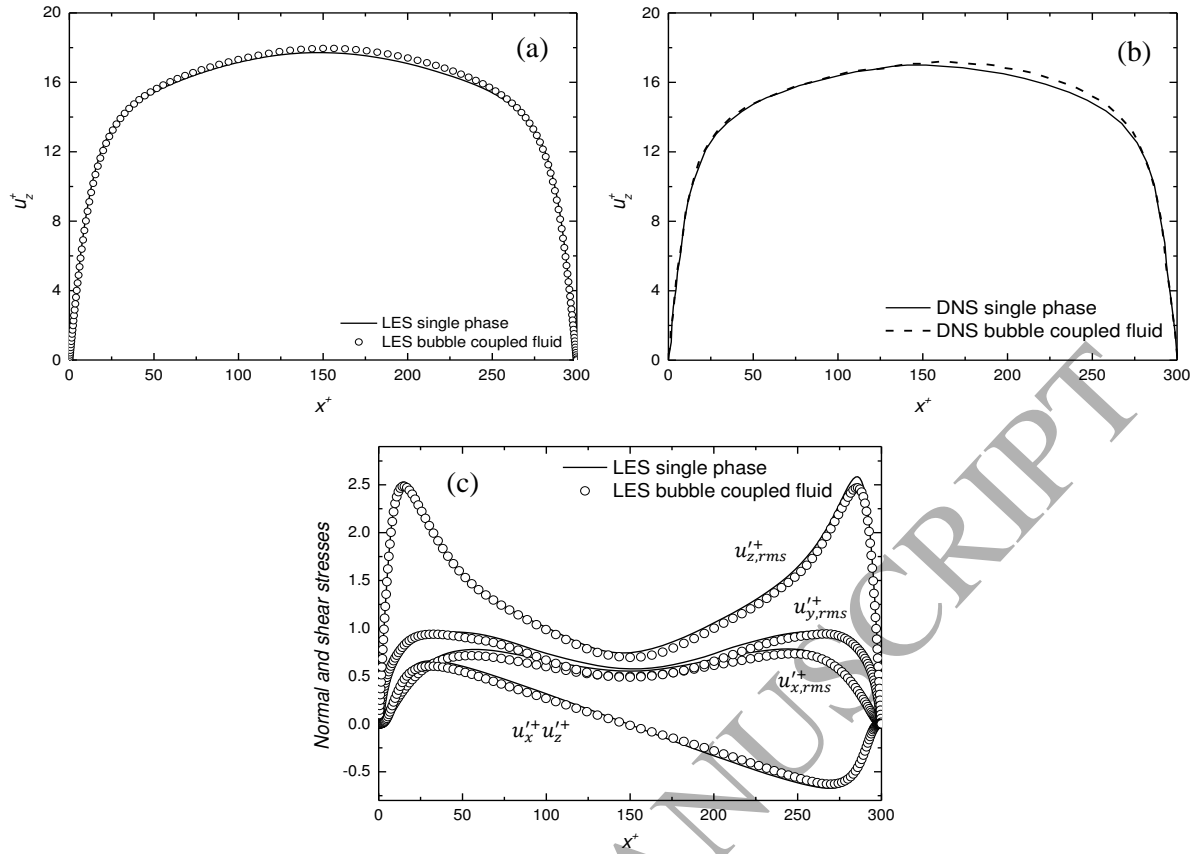


Figure 4. Comparison between two-way coupled and single-phase fluid statistics: (a) LES mean streamwise velocity, (b) DNS mean streamwise velocity (Pang et al., 2014), and (c) LES turbulent normal and shear stresses.

This concentration of bubbles near the upper wall affects the velocity field of the fluid, and a comparison between the two-way coupled and the single-phase fluid mean streamwise velocities and turbulent stresses is given in Fig. 4. The LES mean streamwise velocity is shown in Fig. 4(a) and this can be compared with the DNS prediction from Pang et al. (2014) given in Fig. 4(b). The LES turbulent normal and shear stresses are also shown in Fig. 4(c). Relative to the single-phase, the mean velocity of the fluid phase exhibits an asymmetrical profile. More specifically, in the lower half of the channel ($0 < x^+ < 150$), the fluid velocity generally matches that of the single phase due to the negligible number of microbubbles in that region. In contrast, in the upper half of the channel ($151 < x^+ < 300$), the fluid phase velocity is slightly enhanced in the region away from the wall due to the presence of the microbubbles. As a consequence, the peak velocity is shifted slightly higher than the channel centre relative to the single phase peak. Some small modifications are also visible in the

turbulent stress profiles (Fig. 4(c)) which, in agreement with Pang et al. (2014), are slightly reduced in the upper half of the channel, particularly in the streamwise direction.

4.3 Effect of Reynolds number

Additional simulations at $Re_\tau = 590$ were also made for the two-way coupled LES to study the effect of turbulence levels on microbubble dispersion and migration to the upper wall. Fig. 5 shows the fluid velocity statistics, the bubble velocity statistics and bubble concentration profiles with time. For the fluid, the two-way coupled results are again compared with the single-phase profiles (Fig. 5(a, b)). The asymmetrical profiles which were observed at a shear Reynolds number $Re_\tau = 150$ are not apparent at the higher Reynolds number, with the mean velocity and turbulent stress profiles insignificantly different from the corresponding single-phase results. This is a result of the higher bulk velocity and turbulence levels that dominate the buoyancy effect on the bubbles and their movement towards the upper wall. This is confirmed by the results of Fig. 5(c, d), where the mean velocity and turbulent stresses of the bubbles are almost identical to those of the continuous phase, and of Fig. 5(e, f), which demonstrates that although some effect of buoyancy is apparent with time near the lower channel wall, there is no significant accumulation of bubbles near the upper wall. As a consequence of the higher bubble dispersion by the turbulence, the concentration of bubbles therefore remains high in the upper half of the channel, even at $t^+ = 1200$.

An additional simulation at the intermediate shear Reynolds number of $Re_\tau = 300$ was also performed, and results for the bubble concentration in the channel at all three Reynolds numbers are shown in Fig. 6(a, b). This allows further consideration of the time required for the microbubbles to move from the lower to the upper channel wall, with the predictions in Fig. 6 plotted at a fixed time of $t^+ = 70$ and with distance given relative to the total channel height, H^+ , expressed in wall units. At $Re_\tau = 150$, the microbubble concentration is negligible in the lower regions of the channel until $x^+/H^+ = 0.55$, such that more than half the channel is devoid of bubbles. In contrast, bubbles still occupy the majority of the channel height at $Re_\tau = 300$, and even more so at $Re_\tau = 590$, because of their higher mean velocity and turbulence levels that partially override the buoyancy effect. Comparing the bubble concentration at $Re_\tau = 150$ and $Re_\tau = 590$ at the t^+ used in Fig. 5, the migration rate of the microbubbles is 11 times faster at the lower shear Reynolds number. A correspondingly

lower concentration of bubbles at the upper channel wall with increasing Re_τ is shown in Fig. 6(b).

ACCEPTED MANUSCRIPT

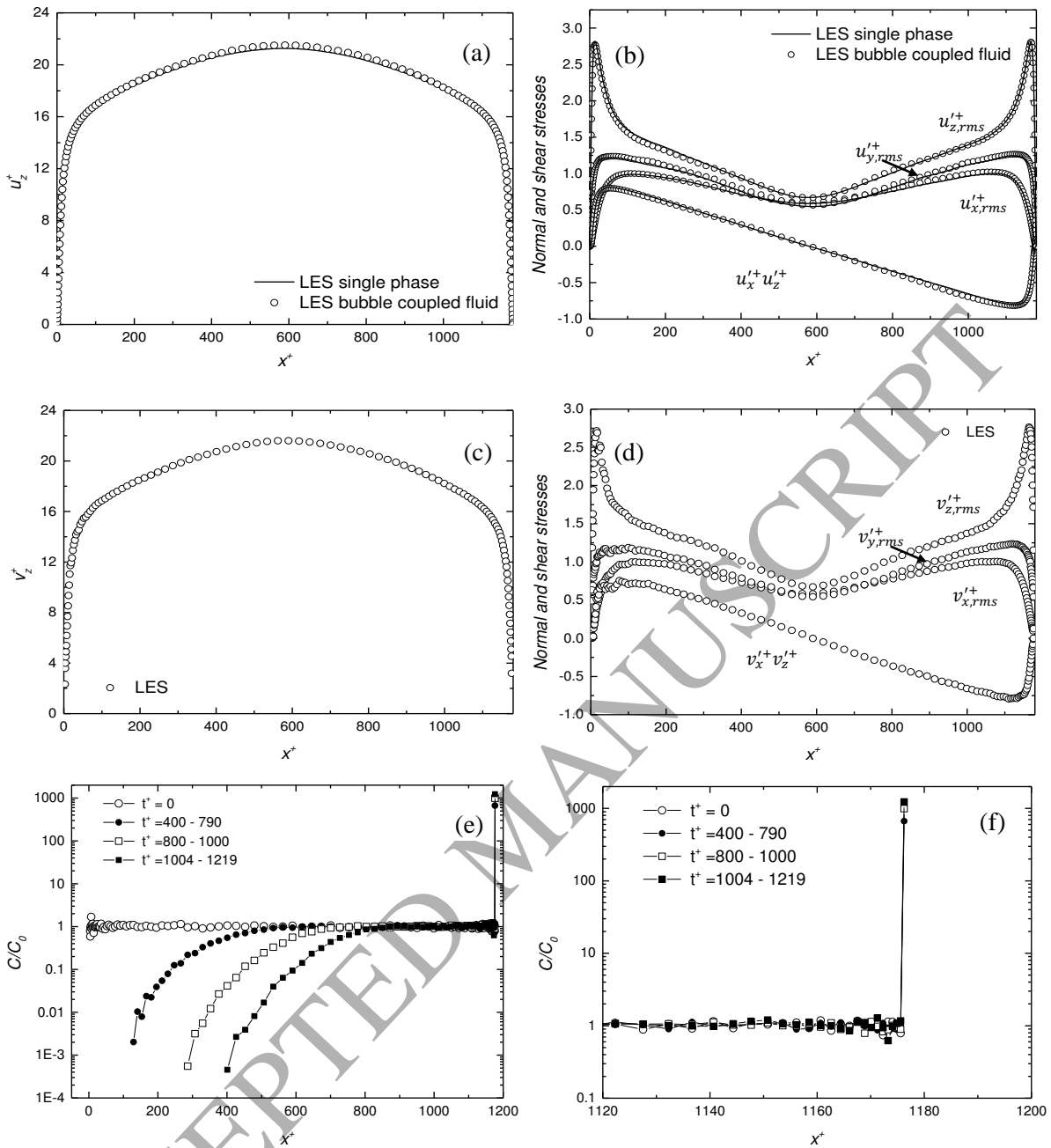


Figure 5. Fluid and bubble velocity statistics at $t^+ = 1219$, and time evolution of bubble concentration profiles, in two-way coupled simulations at $Re_\tau = 590$: (a) fluid mean streamwise velocity compared against the single phase, (b) fluid turbulent normal and shear stresses compared against the single phase, (c) bubble mean streamwise velocity, (d) bubble turbulent normal and shear stresses, (e) bubble concentration profiles across the horizontal channel, and (f) bubble concentration profiles close to the upper channel wall.

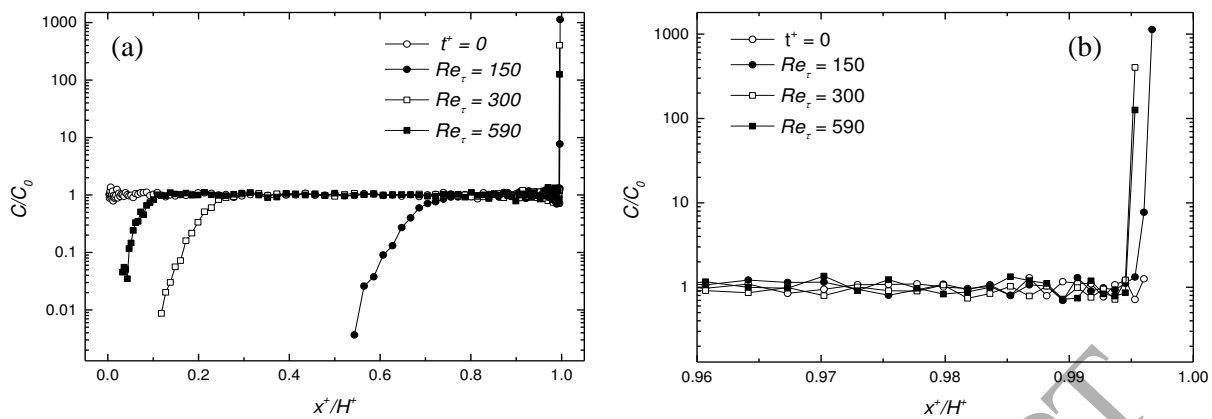


Figure 6. Bubble concentration profiles at $t^+ = 70$ for different shear Reynolds numbers: (a) across the horizontal channel, and (b) close to the upper channel wall.

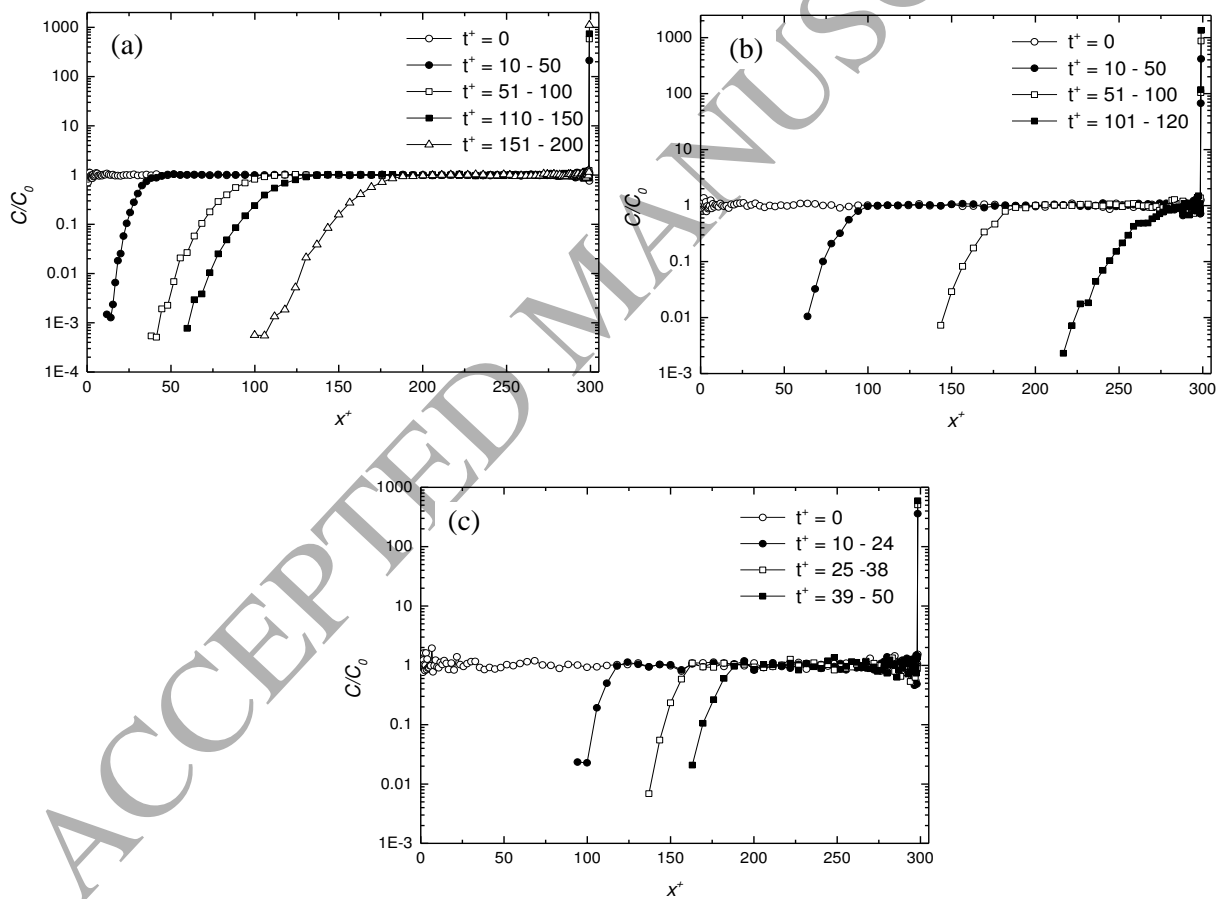


Figure 7. Time evolution of bubble concentration profiles at $Re_\tau = 150$ for different bubble diameters: (a) 110 μm , (b) 220 μm , and (c) 330 μm .

4.4 Effect of microbubble diameter

The influence of bubble size was also studied using two additional bubble diameters ($d_b = 110 \mu\text{m}$ and $330 \mu\text{m}$), with simulations performed at shear Reynolds numbers of 150 and 590. The evolution of bubble concentration profiles at $Re_\tau = 150$ is illustrated in Fig. 7 and at $Re_\tau = 590$ in Fig. 8. Both figures give results for all three bubble sizes considered. In Fig. 7, the segregation of the microbubbles and their movement towards the upper wall is increased with an increase in the bubble size. In Fig. 7(a), some bubbles remain in the lower half of the channel at $t^+ \approx 200$, whilst in Fig. 7(b), the lower half of the channel is practically devoid of bubbles by $t^+ \approx 100$ and by $t^+ \approx 38$ in Fig. 7(c). Since the buoyancy force acting on the bubbles is proportional to their volume, and hence to the third power of the bubble diameter, it is increased eight times by doubling the bubble diameter. In contrast, larger bubbles tend to be less affected by turbulent dispersion. Therefore, the buoyancy force is clearly more influential than turbulent dispersion at the larger bubble diameters, with buoyancy promoting the greater segregation of the bubbles and their accumulation near the upper wall of the channel.

Results for the higher shear Reynolds number are given in Fig. 8. Similar to the results of Fig. 7, the rate of microbubble migration upwards in the channel increases with bubble size, although this increase is slower when compared to the shear Reynolds number $Re_\tau = 150$ flow because of the higher bulk velocity and turbulence levels that increase the dispersion of the microbubbles.

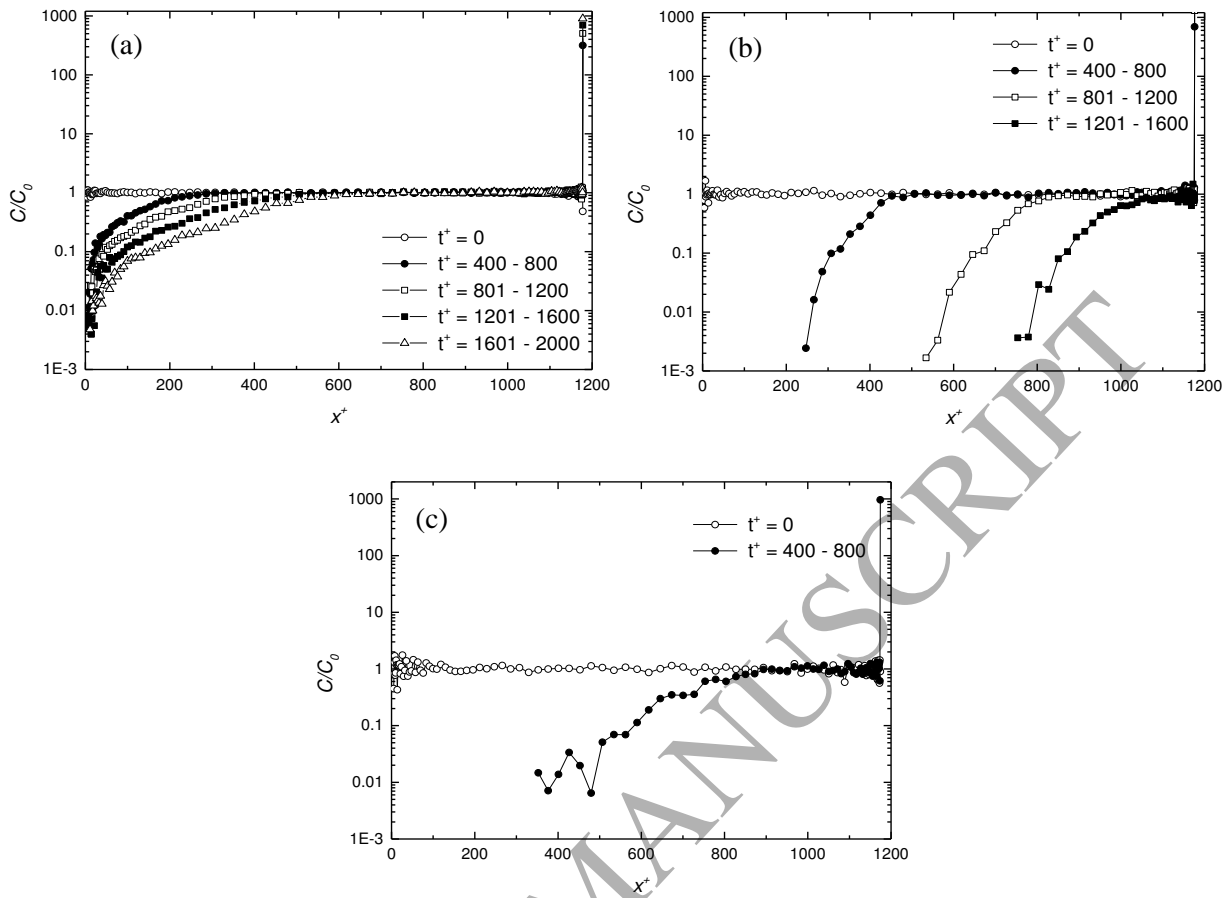


Figure 8. Time evolution of bubble concentration profiles at $Re_\tau = 590$ for different bubble diameters: (a) 110 μm , (b) 220 μm , and (c) 330 μm .

4.5 Forces acting on bubbles in the wall-normal direction

In this section, the individual forces acting on the bubbles are analysed in more detail. More specifically, the forces in the wall-normal direction are considered, in terms of the force per unit mass (N kg^{-1}), since it is in this direction that the greatest change in bubble distribution occurs. In Fig. 9, plots of all the individual forces acting on the bubbles are depicted for the $Re_\tau = 150$ and $Re_\tau = 590$ cases for a bubble diameter $d_b = 220 \mu\text{m}$ and at $t^+ = 200$. Forces are only shown for the upper half of the channel since the trends found there were in the main repeated in the lower half. Also, similar results were found for all three bubble sizes considered and, therefore, only results for the 220 μm case are shown. Fig. 9(a) and (c) shows the wall-normal profiles for all the forces at the two Reynolds numbers considered. In both cases, the gravity-buoyancy force is, as expected, the dominant force with a constant value of 19.6 m s^{-2} in the direction of the upper wall. This force is balanced by drag, with other forces such as lift, added mass and pressure gradient being negligible. Because of their small

magnitudes, Fig. 9(b) and (d) shows an expanded scale to better illustrate the variation in the latter forces. At the higher shear Reynolds number $Re_\tau = 590$ (Fig. 9(c, d)) in particular, although the gravity-buoyancy and drag forces are still dominant, the lift, added mass and pressure gradient forces are seen to play a role, albeit small, in the near-wall region. Here, an increased positive lift contributes to pushing bubbles towards the wall, with a slightly counteracting effect from the added mass and pressure gradient forces also observed. Overall, however, the force analysis shows the dominant role of the gravity-buoyancy force and the balancing effect of the drag force that is generated as soon as the bubbles start to migrate towards the upper surface.

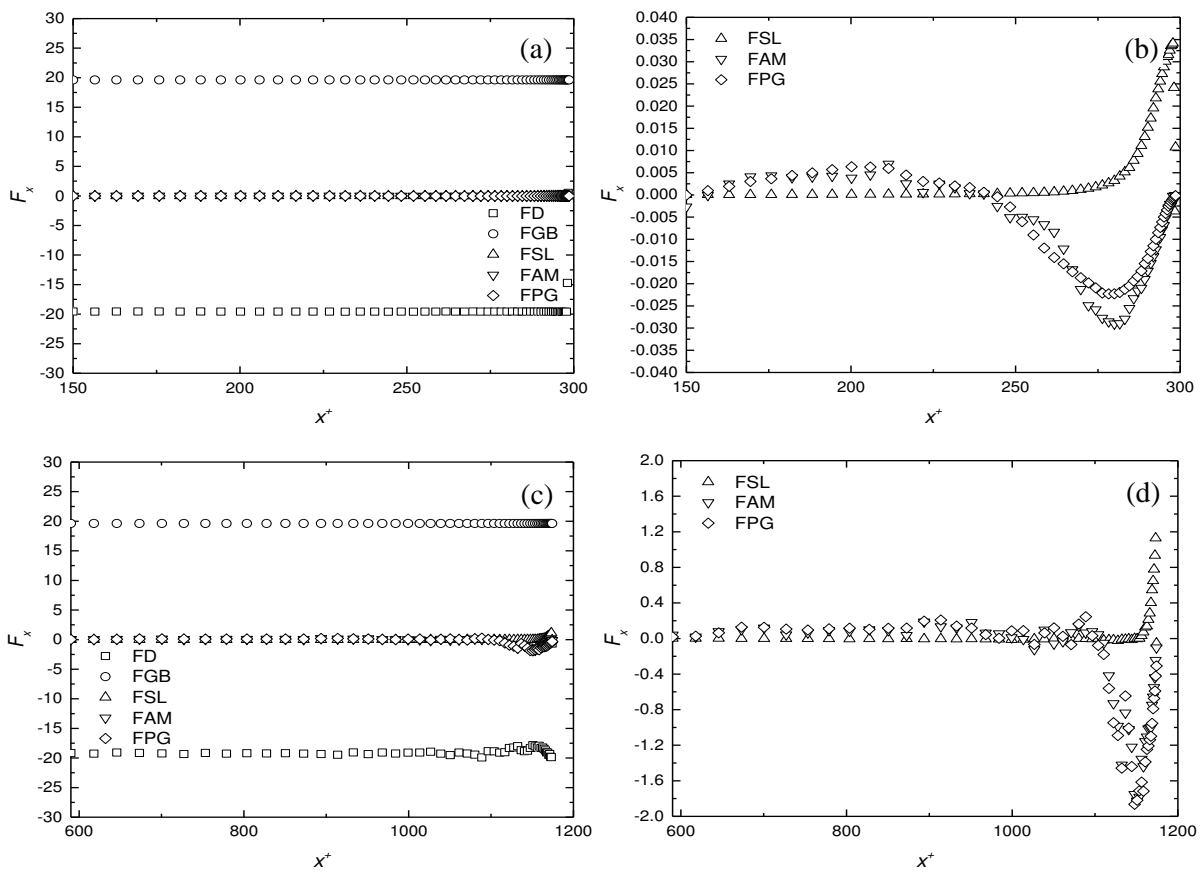


Figure 9. Forces acting in the wall normal direction on $d_b = 220 \mu\text{m}$ bubbles at $t^+ = 200$. (a) and (b) for $Re_\tau = 150$, (c) and (d) for $Re_\tau = 590$. Plots (b) and (d) show an expanded scale to give relative magnitude of smaller forces (FD = drag force, FGB = gravity-buoyancy force, FSL = shear lift force, FAM = added mass force, FPG = pressure gradient force).

4.6 Extent of bubble coalescence

Lastly, results from a simulation made with an extended version of the model that takes into account bubble collision and coalescence are presented. More specifically, results are given from the now four-way coupled model for a shear Reynolds number $Re_\tau = 150$ flow with a bubble size $d_b = 110 \mu\text{m}$. In the various flows considered in this paper, coalescence can be expected to be highest near the upper wall of the channel in regions where turbulence levels are relatively high because the concentration of bubbles in such regions increases due to their migration with time. The rate of migration of bubbles towards the upper wall increases with the bubble diameter and decreasing Reynolds number. However, since the void fraction of the bubbles was the same in all simulations, this means that a significantly larger number of bubbles are present in the flow with the smallest bubble diameter, and such large numbers of bubbles promote collision and coalescence events. For all the flows examined, therefore, bubble coalescence was greatest in the $Re_\tau = 150$ case with a bubble diameter $d_b = 110 \mu\text{m}$.

Results are shown in Fig. 10, where the various plots give the number of collision and coalescence events as a function of time (Fig. 10(a)), the evolution of the bubble population with larger bubbles (consisting of two primary bubbles (2), three primary bubbles (3), etc.) generated by coalescence events (Fig. 10(b)), and the spatial distribution of collision and coalescence events (Fig. 10(c)) and bubbles of any size (Fig. 10(d)). In Fig. 10(a), the number of collisions continuously increases as the simulation progresses and virtually all collision events result in coalescence, with collisions without coalescence only occurring from $t^+ = 190$. This almost 100% coalescence efficiency is due mainly to the low Reynolds number, since the relatively low levels of turbulence in this flow result in high bubble contact times that are sufficient for the liquid film trapped between the bubbles to drain off. As a consequence of the coalescence events, the number of $110 \mu\text{m}$ bubbles reduces over time and progressively more large bubbles, generated by the coalescence of two or more smaller bubbles, are formed. Figure 10(b) shows that bubbles with a volume equivalent of up to five primary bubbles are formed over the time period considered. The spatial distribution of collisions and coalescences is presented in Fig. 10(c), and this confirms a coalescence efficiency of almost 100%. Overall, however, the total number of coalescence events is rather small and, as expected, the largest number of such events occurs near the upper wall where the concentration of the bubbles is highest (Fig. 10(d)). Therefore, the migration of bubbles towards the upper wall can increase coalescence in flows where it might be expected to be insignificant, even though the total number of coalescences was not enough in the case

considered to significantly affect the continuum flow characteristics. As already noted, even lower levels of coalescence were found in the other flows considered above. Nevertheless, the model described will be of value in future work which will consider different flows where coalescence, and bubble break-up, play a more significant role.

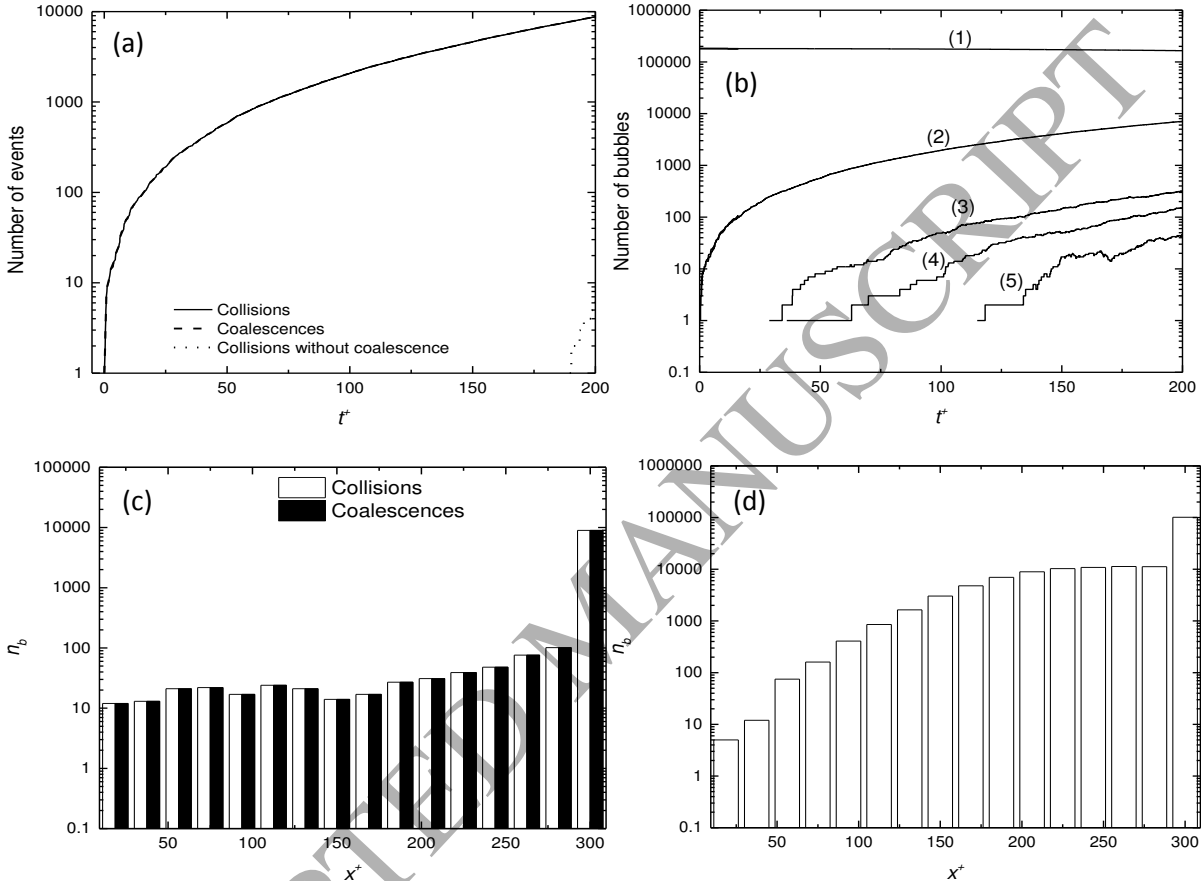


Figure 10. Bubble collision and coalescence statistics for $Re_\tau = 150$ and $d_b = 110 \mu\text{m}$ flow: (a) number of bubble collisions, coalescences and collisions without coalescence, (b) number of bubbles of various sizes formed after coalescence, (c) spatially averaged number of bubble collisions and coalescences with height in the channel at $t^+ = 200$, and (d) number of bubbles (of any size) with height in the channel at $t^+ = 200$.

5. Conclusions

A turbulent flow of water containing air microbubbles in a horizontal channel has been simulated using large eddy simulation coupled with a Lagrangian bubble tracker. The computation was carried out using $128 \times 129 \times 128$ grid nodes for the streamwise, wall normal and spanwise directions, respectively. Results at a shear Reynolds number of 150 and

a bubble diameter of 220 μm show acceptable agreement with the DNS predictions of Pang et al. (2014) for single- and two-phase flows, and in terms of the mean velocity and turbulent stress results available from the latter work. The results show the low density microbubbles migrating towards the upper channel wall with time under the influence of buoyancy, with the accumulation of microbubbles near the upper wall modifying the liquid velocity field such that the mean velocity profile becomes asymmetric, in agreement with DNS predictions (Pang et al., 2014). Some slight modification of the turbulent stresses is also noted. Using the same computational grid, the simulations were extended to a shear Reynolds number $Re_\tau = 590$. At higher mean velocity and turbulence levels, the buoyancy effect is partially overridden by the turbulent dispersion of the microbubbles, which migration towards the upper channel wall significantly reduced as a consequence.

At both shear Reynolds numbers, the influence of microbubble diameter was also investigated, with simulations performed for 110 μm , 220 μm and 330 μm diameter bubbles. Buoyancy, being proportional to the bubble volume, increases bubble migration towards the upper channel wall and segregation of the bubbles in the upper half of the channel with increasing bubble diameter, with this effect reduced with increasing Reynolds number. Predictions made incorporating bubble coalescence effects also confirm that the migration of bubbles towards the upper wall can cause coalescence in flows where it might be expected to be insignificant, even though the total number of coalescences in the flows considered was not large enough or sufficient to significantly affect the continuum flow characteristics.

Overall, the LES and Lagrangian bubble tracker are able to reproduce the turbulent flow, dispersion and concentration of microbubbles in a horizontal channel. More specifically, LES captures with a sufficient level of detail the flow structures that are responsible for interactions with microbubbles and that affect bubble behaviour. Therefore, the present model can be used with confidence to predict not only channel flows, but other flow configurations and conditions that are of engineering interest. Application of these techniques to upward and downward flows in vertically orientated channels is underway, as is an extension of the model described to consider bubble break-up due to shear effects. These flows will be used to consider bubble coalescence and break-up in more detail due to the increased prevalence of coalescence in this flow configuration.

Acknowledgements

KSA gratefully acknowledges the financial support of the Niger Delta Development Commission in Nigeria, and the opportunities that funding has given him.

References

- Apte, S.V., Mahesh, K., Lundgren, T., 2003. A Eulerian-Lagrangian model to simulate two-phase/particulate flows. Center for Turbulence Research, Annual Research Briefs, 161-171.
- Auton, T.R., 1987. The lift force on a spherical body in a rotational flow. *J. Fluid Mech.* 183, 199-218.
- Auton, T.R., Hunt, J.C.R., Prud'Homme, M., 1988. The force exerted on a body in inviscid unsteady non-uniform rotational flow. *J. Fluid Mech.* 197, 241-257.
- Bini, M., Jones, W.P., 2008. Large-eddy simulation of particle-laden turbulent flows. *J. Fluid Mech.* 614, 207-252.
- Breuer, M., Alletto, M., 2012. Efficient simulation of particle-laden turbulent flows with high mass loadings using LES. *Int. J. Heat Fluid Flow* 35, 2-12.
- Ceccio, S.L., 2010. Friction drag reduction of external flows with bubble and gas injection. *Annu. Rev. Fluid Mech.* 42, 183-203.
- Deen, N.G., Solberg, T., Hjertager, B.H., 2001. Large eddy simulation of the gas-liquid flow in a square cross-sectioned bubble column. *Chem. Eng. Sci.* 56, 6341-6349.
- Delnoij, E., Lammers, F.A., Kuipers, J.A.M., van Swaaijet, W.P.M., 1997. Dynamic simulation of dispersed gas-liquid two-phase flow using a discrete bubble model. *Chem. Eng. Sci.* 52, 1429-1458.
- de Vries, A.W.G., Biesheuvel, A., van Wijngaarden, L., 2002. Notes on the path and wake of a gas bubble rising in pure water. *Int. J. Multiphase Flow* 28, 1823-1835.
- di Mare, L., Jones, W.P., 2003. LES of turbulent flow past a swept fence. *Int. J. Heat Fluid Flow* 24, 606-615.
- di Mare, F., Jones, W.P., Menzies, K.R., 2004. Large eddy simulation of a model gas turbine combustor. *Combust. Flame* 137, 278-294.
- Elghobashi, S., Truesdell, G.C., 1992. Direct simulation of particle dispersion in a decaying isotropic turbulence. *J. Fluid Mech.* 242, 655-700.

- Ellingsen, K., Risso, F., 2001. On the rise of an ellipsoidal bubble in water: oscillatory paths and liquid-induced velocity. *J. Fluid Mech.* 440, 235-268.
- Ervin, E.A., Tryggvason, G., 1997. The rise of bubbles in a vertical shear flow. *J. Fluids Eng.* 119, 443-449.
- Esmaeeli, A., Ervin, E., Tryggvason, G., 1994. Numerical simulations of rising bubbles, in: Blake, J.R., Boulton-Stone, J.M., Thomas, N.H. (Eds.), *Bubble Dynamics and Interface Phenomena: Proceedings of IUTAM Symposium, Birmingham, U.K., 6-9 September 1993*. Springer Netherlands, Dordrecht, pp. 247-255.
- Esmaeeli, A., Tryggvason, G., 1998. Direct numerical simulations of bubbly flows. Part 1. Low Reynolds number arrays. *J. Fluid Mech.* 377, 313-345.
- Ferrante, A., Elghobashi, S., 2004. On the physical mechanisms of drag reduction in a spatially-developing turbulent boundary layer laden with microbubbles. *J. Fluid Mech.* 503, 345-355.
- Gamet, L., Ducros, F., Nicoud, F., Poinso, T., 1999. Compact finite difference schemes on non-uniform meshes. Application to direct numerical simulations of compressible flows. *Int. J. Numer. Meth. Fl.* 29, 159-191.
- Germano, M., Piomelli, U., Moin, P., Cabot, W.H., 1991. A dynamic subgrid-scale eddy viscosity model. *Phys. Fluids A* 3, 1760-1765.
- Giusti, A., Lucci, F., Soldati, A., 2005. Influence of the lift force in direct numerical simulation of upward/downward turbulent channel flow laden with surfactant contaminated microbubbles. *Chem. Eng. Sci.* 60, 6176-6187.
- Göz, M.F., Bunner, B., Sommerfeld, M., Tryggvason, G., 2002. Direct numerical simulation of bubble swarms with a parallel front-tracking method, in: Breuer, M., Durst, F., Zenger, C. (Eds.), *High Performance Scientific and Engineering Computing*. Springer Berlin, pp. 97-106.
- Hassan, A., 2014. Bubbly two-phase flow: Part II - Characteristics and parameters. *Am. J. Fluid Dyn.* 4, 115-180.
- Hibiki, T., Ishii, M., 2007. Lift force in bubbly flow systems. *Chem. Eng. Sci.* 62, 6457-6474.
- Jeong, H., Park, H., 2015. Near-wall rising behaviour of a deformable bubble at high Reynolds number. *J. Fluid Mech.* 771, 564-594.

- Jones, W.P., Marquis, A.J., Vogiatzaki, K., 2014. Large-eddy simulation of spray combustion in a gas turbine combustor. *Combust. Flame* 161, 222-239.
- Kitagawa, A., Hishida, K., Kodama, Y., 2005. Flow structure of microbubble-laden turbulent channel flow measured by PIV combined with the shadow image technique. *Exp. Fluids* 38, 466-475.
- Lau, Y.M., Bai, W., Deen, N.G., Kuipers, J.A.M., 2014. Numerical study of bubble break-up in bubbly flows using a deterministic Euler-Lagrange framework. *Chem. Eng. Sci.* 108, 9-22.
- Legendre, D., Magnaudet, J., 1997. A note on the lift force on a spherical bubble or drop in a low-Reynolds-number shear flow. *Phys. Fluids* 9, 3572-3574.
- Lighthill, M.J., 1956. The lift force on a spherical rotational flow. *J. Fluid Mech.* 1, 31-53.
- Lilly, D.K., 1967. The representation of small scale turbulence in numerical simulation experiments, in: Goldstine, H.H. (Ed.), *Proc. IBM Scientific Computing Symposium on Environmental Sciences*. Yorktown Heights, New York, pp. 195-210.
- Lu, A., Fernandez, J., Tryggvason, G., 2005. The effect of bubbles on the wall drag in a turbulent channel flow. *Phys. Fluids* 17, 095102.
- Marchioli, C., Soldati, A., Kuerten, J.G.M., Arcen, B., Tanière, A., Goldensohn, G., Squires, K.D., Cargnelutti, M.F., Portela, L.M., 2008. Statistics of particle dispersion in direct numerical simulations of wall-bounded turbulence: Results of an international collaborative benchmark test. *Int. J. Multiphase Flow* 34, 879-893.
- Maxey, M.R., Riley, J.J., 1983. Equation of motion for a small rigid sphere in a nonuniform flow. *Phys. Fluids* 26, 883-889.
- Mazzitelli, I.M., Lohse, D., Toschi, F., 2003. The effect of microbubbles on developed turbulence. *Phys. Fluids* 15, L5-L8.
- Molin, D., Marchioli, C., Soldati, A., 2012. Turbulence modulation and microbubble dynamics in vertical channel flow. *Int. J. Multiphase Flow* 42, 80-95.
- Moser, R.D., Kim, J., Mansour, N.N., 1999. Direct numerical simulation of turbulent channel flow up to $Re_\tau=590$. *Phys. Fluids* 11, 943-945.
- Murai, Y., 2014. Frictional drag reduction by bubble injection. *Exp. Fluids* 55, 1-28.
- Njobuenwu, D.O., Fairweather, M., 2015. Dynamics of single, non-spherical ellipsoidal particles in a turbulent channel flow. *Chem. Eng. Sci.* 123, 265-282.

- Njobuenwu, D O., Fairweather, M., 2017. Simulation of deterministic energy-balance particle agglomeration in turbulent liquid-solid flows. arXiv preprint arXiv:1701.02346.
- Njobuenwu, D.O., Fairweather, M., Yao, J., 2013. Coupled RANS–LPT modelling of dilute, particle-laden flow in a duct with a 90° bend. *Int. J. Multiphase Flow* 50, 71-88.
- Paik, B.-G., Yim, G.-T., Kim, K.-Y., Kim, K.-S., 2016. The effects of microbubbles on skin friction in a turbulent boundary layer flow. *Int. J. Multiphase Flow* 80, 164-175.
- Pang, M.J., Wei, J.J., Yu, B., 2014. Numerical study on modulation of microbubbles on turbulence frictional drag in a horizontal channel. *Ocean Eng.* 81, 58-68.
- Piomelli, U., Liu, J., 1995. Large-eddy simulation of rotating channel flows using a localized dynamic model. *Phys. Fluids* 7, 839-848.
- Porte-Agel, F., Meneveau, C., Parlange, M., 2000. A scale-dependent dynamic model for large eddy simulation: Application to a neutral atmospheric boundary layer. *J. Fluid Mech.* 415, 261-284.
- Prince M.J., Blanch, H.W., 1990. Bubble coalescence and break-up in air-sparged bubble-columns. *AIChE J.* 36, 1485-1499.
- Rivero, M., Magnaudet, J., Fabre, J., 1991. New results on the forces exerted on a spherical body by an accelerated flow. *C. R. Acad. Sci. Paris Ser. II*, 312, 1499-1506.
- Schiller, L., Naumann, Z., 1935. A drag coefficient correlation. *Z. Ver. Deutsch. Ing.*, 77, 318-323.
- Sommerfeld, M., Bourloutski, E., Brüder, D., 2003. Euler/Lagrange calculations of bubbly flows with consideration of bubble coalescence. *Can. J. Chem. Eng.* 81, 508-518.
- Sridhar, G., Katz, J., 1999. Effect of entrained bubbles on the structure of vortex rings. *J. Fluid Mech.* 397, 171-202.
- van den Hengel, E.I.V., Deen, N.G., Kuipers, J.A.M., 2005. Application of coalescence and breakup models in a discrete bubble model for bubble columns. *Ind. Eng. Chem. Res.* 44, 5233-5245.
- Wang, L.-P., Maxey, M.R., 1993. Settling velocity and concentration distribution of heavy particles in homogeneous isotropic turbulence. *J. Fluid Mech.* 256, 27-68.
- Wang, S.K., Lee, S.J., Jones, O.C., Lahey, R.T., 1987. 3-D turbulence structure and phase distribution measurements in bubbly two-phase flows. *Int. J. Multiphase Flow* 13, 327-343.

Watanabe, T., Tasaka, Y., Murai, Y., 2013. Intensified and attenuated waves in a microbubble Taylor–Couette flow. *Phys. Fluids* 25, 054107.

Wörner, M., 2012. Numerical modeling of multiphase flows in microfluidics and micro process engineering: a review of methods and applications. *Microfluid. Nanofluidics* 12, 841-886.

Xu, J., Maxey, M.R., Karniadakis, G.E., 2002. Numerical simulation of turbulent drag reduction using micro-bubbles. *J. Fluid Mech.* 468, 271-281.

Yamamoto, Y., Potthoff, M., Tanaka, T., Kajishima, T., Tsuji, Y., 2001. Large-eddy simulation of turbulent gas–particle flow in a vertical channel: effect of considering inter-particle collisions. *J. Fluid Mech.* 442, 303-334.

ACCEPTED MANUSCRIPT